I&EC research
Industrial & Engineering Chemistry Research

pubs.acs.org/IECR

Article

Performance of Pt/Cr_2O_3, Pt/ZrO_2, and, $Pt/\gamma\text{-}Al_2O_3$ Catalysts in Total Oxidation of Methane: Effect of Metal–Support Interaction

Grisel Corro,* Jorge Cruz-Mérida, Daniel Montalvo, and Umapada Pal

Cite This: *Ind. Eng. Chem. Res.* 2021, 60, 18841−18852

Read Online

ACCESS | Metrics & More | Article Recommendations | Supporting Information

ABSTRACT: We present the catalytic performance of Pt-supported Cr_2O_3, and ZrO_2 (semiconductors), and $\gamma\text{-}Al_2O_3$ (insulator) in CH_4 oxidation under lean conditions. XPS analysis of the catalysts showed only Pt^{2+} at the $Pt/\gamma\text{-}Al_2O_3$ surface, and stable Pt^x-Pt^y dipolar catalytic sites at the surface of Pt/Cr_2O_3 and Pt/ZrO_2. The presence of such dipolar moieties increases the polarization probability of methane molecules, resulting in an increment of the molecule's kinetic energy and in an increase of the strength of its impact with the catalyst surface, weakening the C−H bond energy and enhancing hydrogen detachment from CH_4 adsorbed molecules. The detachment of this hydrogen is the rate-determining step of the reaction. The formation and stability of the Pt^x-Pt^y dipolar moieties have been related to the electronic effects associated with platinum and metal oxide semiconductor support interactions. Results reported in this investigation demonstrate the possibility of tuning the catalytic activity of Pt supported on metal oxides for methane oxidation by controlling the nature of the Pt^x-Pt^y dipolar moieties at the surface of metal oxide supports by selecting the semiconducting supports of suitable work functions.

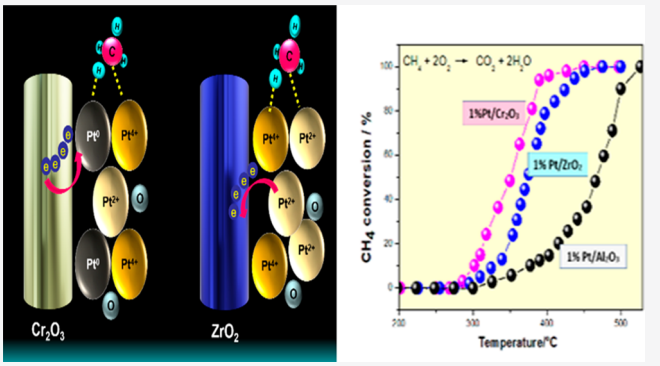

INTRODUCTION

The main focus of current research on internal combustion engines is the reduction of carbon dioxide (CO_2) emission through their exhaust to the environment. In this aspect, gas-fed lean-burn engines are exceptional substitutes to the traditional gasoline or diesel engines, because of their economic and environmental benefits, since they utilize natural gas and biogas as fuels. One of the principal environmental benefits of utilizing natural gas and biogas as fuels is their efficient combustion in oxygen-rich ambient environments and the generation of relatively lower amounts of CO_2 per unit of combustion heat. Moreover, under optimum combustion conditions, it produces only a negligible amount of carbon soot, even without a considerable fuel penalty.[1]

Natural gas is a mixture of hydrocarbon gases. It is formed primarily of methane (typically 70%−90%), ethane, propane, butane, and pentane (up to 20% in some deposits) and other gases such as CO_2, O_2, N_2, and H_2S (0−5%).[2] In addition, natural gas and biogas are abundant and inexpensive. However, methane, the main component of natural gas, is a dangerous greenhouse gas.[3] Therefore, during natural gas or biogas combustion, a low level of methane emission must be guaranteed.

Catalytic exhaust aftertreatment technologies must be considered to abate methane from the exhaust, because methane emission regulations are being tightened and engine modifications alone are unable to comply with them. Therefore, the challenge is to develop catalysts that are active for the total oxidation of methane under lean conditions, around the same temperature as that of the exhaust. However, the task is complicated further by the presence of sulfur molecules that deactivate many catalytic aftertreatment systems.

The complete oxidation of methane can be expressed as

$$CH_4 + 2O_2 \rightarrow CO_2 + 2H_2O \quad \text{(R1)}$$

that is highly exothermic, with $\Delta H_{rxn} = -891$ kJ/mol.[4] Nevertheless, the activation energy of the reaction is considerable. The limiting step of this reaction is the abstraction of the first H atom from CH_4 molecule, requiring 430 kJ/mol.[5] The reaction happens spontaneously at 1000 °C.[6] However, an oxidation catalyst can bring down this temperature considerably.

It is well-known that the best catalyst for total oxidation of methane is palladium. This metal, supported on metal oxides, under lean conditions, exhibited a temperature for CH_4 oxidation of <450 °C. This temperature has been the lowest reported for the methane oxidation.[7−9] However, catalysts

Special Issue: José Luis García Fierro Festschrift

Received: July 22, 2021
Revised: November 15, 2021
Accepted: November 16, 2021
Published: November 24, 2021

containing palladium are redispersed under reoxidation, reduced at high temperatures, and deactivated by water produced during the combustion of hydrocarbons present in natural gas and biogas, or even by small amounts (1 ppm) of sulfur containing species in the exhaust.[10] The concentration of these sulfur containing species may be lowered through natural gas purification. However, the gas purification process is expensive.

Sulfur species cause deactivation of the oxidation active sites of palladium catalysts through the formation of palladium sulfates, which are highly stable species.[10−12] Moreover, the regeneration of palladium-based catalysts after sulfur deactivation is challenging, requiring high temperatures, rich fuel mixture operation, or both.[13]

Other catalysts such as single-metal oxides, perovskites, and spinels have also been investigated for CH_4 total oxidation.[14−16] However, most of these catalysts have not shown the benefits of Pd-based systems. Recently, rhodium/ZSM-5 has been reported as a highly active CH_4 oxidation catalyst, resistant to H_2O and SO_2. However, the high cost of Rh should be considered for its large-scale application.[17]

Platinum-based catalysts are strongly active for oxidative elimination of hydrocarbons from exhausts in small quantities.[18,19] However, in the particular case of methane, apart from palladium, Pt is also considered as one of the highly active catalytic species for the oxidation of hydrocarbons. Under lean conditions, platinum-based catalysts can oxidize CH_4 at temperatures of >500 °C.[4,11] However, unlike palladium-based catalysts, they are not deactivated by water or by the presence of other hydrocarbons in the gas mixture. As has been stated earlier, the composition of natural gas includes methane, along with other hydrocarbons (ethane, propane, butane, and pentane). Platinum-based catalysts are able to oxidize the other hydrocarbons more effectively and at lower temperatures than palladium-based catalysts.[11,18] Therefore, it is challenging to find a platinum-based catalyst that is capable of oxidizing not only methane, but also the other hydrocarbons present in natural gas. Not only are the platinum-based catalysts more sulfur-resistant than palladium-based catalysts,[11] as has been demonstrated by Kylhammar et al., but SO_2 also promotes the total oxidation of methane over Pt-based metal oxide catalysts, such as ceria, under oxygen excess conditions.[20]

Now, the activity of platinum-based catalysts is dependent on the reactant gas composition.[10,11] Particularly, for the Pt/Al_2O_3 catalyst, the methane oxidation is inhibited under excess oxygen.[10−12,21−26] Therefore, the first objective of the present investigation is to determine the possibility of developing a platinum-based catalyst, which can preferentially adsorb methane under excess oxygen conditions, preventing methane oxidation inhibition.

Because of the high level of structural symmetry and low molecular polarizability, methane molecules require high energy to overcome the adsorption activation energy at the striking catalyst surface. Therefore, normally, the adsorption of methane molecules at the catalyst surface occurs at relatively higher temperatures. An alternative strategy for increasing the methane adsorption rate on the catalyst surface is to increase the electrostatic attractive force between methane molecules and the catalytic sites, which is possible only by developing dipolar catalytic sites. Gaseous methane molecules, despite their low molecular polarizability, get polarized by the strong inductive interaction with the dipolar catalytic sites and adsorbed on the catalyst surface acquiring the required activation energy.

The adsorption of methane is the controlling step for catalytic CH_4 oxidation. Therefore, the second objective of this investigation is to provide the insight of the formation of Pt^x−Pt^y dipolar sites at the metal/semiconductor interface. These dipolar catalytic sites may increase the total energy of the methane colliding molecules, generating their polarization, thereby decreasing the C−H bond energy and resulting in the H-atom abstraction. Since the development of different valence states of metal ions is largely influenced by the electron transfer process between the metal and its supporting metal oxide,[27] we examined the different valence states of platinum in Pt/Cr_2O_3, Pt/ZrO_2 (Cr_2O_3 and ZrO_2 are semiconductors), and Pt/γ-Al_2O_3 (γ-Al_2O_3 is an insulator).

The electronic and structural characteristics of the catalysts were determined using high-resolution transmission electronic microscopy (HR-TEM) and X-ray photoelectron spectroscopy (XPS). The catalytic behavior of the 1% Pt/Cr_2O_3, 1% Pt/ZrO_2, and 1% Pt/γ-Al_2O_3 catalysts in the oxidation of CH_4 has been associated with the valence state of Pt surface species by the side of the electronic effects between platinum and the metal oxide supports.

EXPERIMENTAL SECTION

Catalyst Preparation. The supports used to elaborate the platinum-supported catalysts were commercial Cr_2O_3, ZrO_2, and γ-Al_2O_3 powders (Aldrich, 99.99%). The catalysts were prepared by incipient impregnation. The process consisted in mixing 5 g of the chosen support with a measured volume of a solution of chloroplatinic acid hexahydrate (Aldrich, 99.99%) to obtain nominal 1 wt % Pt/support. The mixture was stirred magnetically for 1 h at room temperature and the catalyst was recuperated by filtration. The samples were washed thoroughly with deionized water to remove chlorine and dried at 120 °C for 12 h. The resulting powder was calcined at 600 °C in a tubular programmable furnace, for 4 h, under air flow (100 mL min^{-1}). The samples were cooled down to 25 °C under air flow and kept in hermetic glass flasks. Pure Cr_2O_3, ZrO_2, and γ-Al_2O_3 catalysts were also thermally treated under similar conditions to utilize them as references.

Catalyst Characterization. The nitrogen physisorption isotherms of the catalysts were recorded employing a Belsorp Mini-II (BELL, Japan) sorptometer. All the samples were degasified for 2 h at 400 °C before acquiring their isotherms. From the N_2 physisorption at −196 °C, using BET analysis, the specific surface area (S_g) of the catalysts was measured. The physisorption isotherms were acquired in the 0.0−6.6 kPa pressure range. The saturation adsorption was established applying the back extrapolation method of the linear portion of the adsorption isotherms to zero pressure.

XPS spectra were recorded on fresh samples and after the oxidation cycles, employing an Escalab 200R electron spectrometer. The spectrometer was equipped with a hemispherical analyzer that operates in a steady pass energy mode. For acquiring the XPS spectra of the catalysts, it utilized a monochromatic Mg Kα emission ($h\nu$ = 1253.6 eV) from the X-ray tube that operates at 10 mA and 12 kV. The relevant energy sections of the photoelectrons were scanned a convenient number of times with the objective of getting excellent signal-to-noise ratios. The intensities of the emission peaks were estimated by integrating the area under each peak. The integration was performed after the subtraction of an S-

https://doi.org/10.1021/acs.iecr.1c02902
Ind. Eng. Chem. Res. 2021, 60, 18841−18852

shaped background and fitting the obtained peak to Lorentzian/Gaussian curves (80% Lorentzian/20% Gaussian). The C 1s signal, generated from adventitious carbon, was detected at ~284.9 ± 0.2 eV. This position was utilized to reference the peak positions of selected elements.

The high-resolution transmission electron microscopy (HR-TEM) study of the platinum supported samples was performed in a JEOL Model JEM-ARM200CF microscopy system. The images of the catalysts were acquired using the fresh samples and after having used them for the oxidation cycles. Before the HR-TEM study, the catalysts were dispersed in ethanol. This dispersion was deposited over carbon-coated copper grids. The size distribution histograms of the supported platinum nanoparticles were fixed by considering the sizes of 150−200 platinum nanoparticles of each catalyst in their microscopic images.

To verify the formation of dipoles at the surface of the metal oxide supports, because of the incorporation of Pt, we studied the induced resonance Raman optical activity (IRROA) of the samples. A Horiba LabRam HR system provided with a 633 nm He−Ne laser and a thermoelectrically cooled charge-coupled device (CCD) detector was used for acquiring the Raman spectra of the samples. MicroRaman spectra of the catalysts were acquired using suitable objective lenses (50×) and neutral density filters to prevent their laser-induced damage. The intensity of the laser beam and its spot size (diameter) over the samples were 5.75 mW/cm^2 and 8.0 μm, respectively.

Methane Oxidation Catalytic Tests. Catalytic CH_4 total oxidation tests were conducted in a flow reactor at atmospheric pressure. Gas flow rates were regulated with mass flow controllers. The reacting feed gas was a mixture of CH_4 (0.2 vol %), O_2 (10 vol %), and N_2 (balance). The reacting gas flow rate was 100 cm^3 min^{-1}. In order to hinder unwanted heat-transfer shortcomings, the catalyst sample (200 mg) was mixed with 1.0 g of quartz powder. The mixture was placed in a vertical tubular (10 mm inner diameter) quartz reactor. The reactor was positioned in a furnace. A Type K thermocouple was used to monitor the inner temperature of the reactor. To determine CH_4, CO, CO_2, and H_2O concentrations at the reactor outlet, as a function of the reaction temperature, a Shimadzu gas chromatograph that was provided with a thermoconductivity detector was utilized.

Catalytic CH_4 oxidation processes were followed by determining the progress of methane conversion, as a function of temperature (light-off curves). Before beginning the experiments, the catalysts were pretreated at 500 °C for 1 h in the reactant stream. After 1 h of pretreatment, keeping the same reactant flow, the catalysts were cooled to 25 °C.

Methane Oxidation Catalytic Cycle. The temperature range in which the catalytic oxidation of CH_4 was studied was 25−500 °C. The heating rate of the programmable furnace was 2 °C min^{-1}. This rate permitted sufficient time to get to a steady state for every evaluation temperature. When the temperature reached 500 °C, the sample was cooled to 25 °C. A reaction cycle is defined as the entire process of CH_4 oxidation from 25 °C to 500 °C and cooling to 25 °C. The light-off curves enabled us to establish the temperature at which the conversion of methane reached 10% (labeled as T_{10}), 50% (labeled as T_{50}), and 100% (labeled as T_{100}). The presence of H_2O in the effluent was confirmed without quantification. During the entire experiment, CO was not detected in the effluent.

RESULTS AND DISCUSSION

Catalyst Characterization. *Catalyst Specific Surface Area.* The specific surface areas of the 1% Pt/Cr_2O_3, 1% Pt/ZrO_2, and 1% Pt/γ-Al_2O_3 composite catalysts and respective metal oxide supports were evaluated from their N_2 physisorption isotherms performed at −196 °C, before and after their utilization in methane oxidation cycles. The results presented in Table S1 in the Supporting Information indicate that there is no significant change in the specific surface area of the catalysts after their utilization in methane oxidation cycles.

XPS Analysis of the Catalysts. With the view of determining the possible development of dipolar sites at the catalyst surface, and the interactions of these dipolar sites of the catalysts with methane and oxygen molecules during methane oxidation, the electronic properties of the platinum supported catalysts were studied by XPS (Figures 1−4). The binding energy (BE) values of the components and Pt/Cr, Pt/Zr, and Pt/Al atomic ratios determined in the fresh catalysts surface and after using them in methane oxidation cycles, are shown in Table 1.

Table 1. Binding Energy Values of the Components and the Atomic Ratios Pt/Cr, Pt/Zr, and, Pt/Al at the Catalysts Surface, before (Fresh) Samples and after Having Used Them for the Oxidation Cycles (Used)[a]

	Binding Energy (eV)			
catalyst	Pt $4f_{7/2}$	Cr $2p_{3/2}$	Pt $4d_{5/2}$	Pt/Cr atomic ratio
1% Pt/Cr_2O_3 (fresh)	71.6 (9)	576.4	314.1 (12)	0.34
	74.6 (91)		317.0 (80)	
			318.6 (8)	
1% Pt/Cr_2O_3 (used)	71.5 (10)	576.4	314.0 (12)	0.35
	74.7 (90)		316.9 (80)	
			318.6 (8)	
	Binding Energy (eV)			
catalyst	Pt $4f_{7/2}$	Zr $3d_{5/2}$		Pt/Zr atomic ratio
1% Pt/ZrO_2 (fresh)	73.3 (70)	182.2		0.14
	75.3 (30)			
1% Pt/ZrO_2 (used)	73.1 (69)	182.1		0.13
	75.2 (31)			
	Binding Energy (eV)			
catalyst	Al 2p	Pt $4d_{5/2}$		Pt/Al atomic ratio
1% Pt/γ-Al_2O_3 (fresh)	74.4	317.2 (100)		0.31
1% Pt/γ-Al_2O_3 (used)	74.5	317.2 (100)		0.32

[a]The % peak area of Pt^0, Pt^{2+}, and Pt^{4+} components are presented in parentheses.

XPS Evaluation of the 1% Pt/Cr_2O_3 Catalyst. The XPS survey spectrum (not presented) of 1% Pt/Cr_2O_3 fresh sample, revealed characteristic emissions of Pt, Cr, and O, along with the signal of adventitious carbon C, as expected for the composite catalyst. As the objective of XPS analysis of the sample was to determine the valence states of the Pt and Cr metal ions, we analyzed the corresponding core-level emissions of the samples carefully. As can be noticed in Figure 1a, the core-level XPS spectrum disclosed, at ~576 eV, a single component Cr $2p_{3/2}$ band corresponding to Cr^{3+} state.[28−30] On the other hand, the Pt $4f_{7/2}$ emission, presented in Figure 1b, disclosed a small intensity component appearing at ~71.6

https://doi.org/10.1021/acs.iecr.1c02902
Ind. Eng. Chem. Res. 2021, 60, 18841−18852

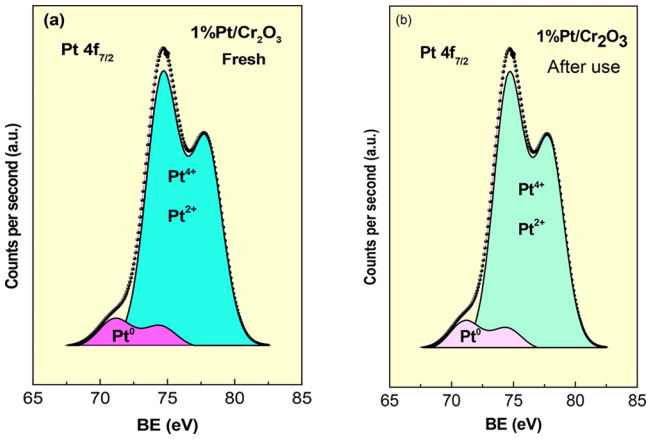

Figure 1. Pt $4f_{7/2}$ core level XPS spectra of the (a) fresh and (b) used (in 6 cycles of methane oxidation) 1% Pt/Cr_2O_3 catalyst.

eV and a relatively intense component at ~74.6 eV. While the 71.6 eV component is associated with Pt^0, the latter component has been attributed to the Pt^{2+} state[31,32] or to Pt^{4+}.[33−35]

Although the binding energy values of Pt^{2+} and Pt^{4+} are pretty close, and the capacity of the spectrometer did not permit to differentiate the components categorically, the broad and asymmetric nature of the emission band suggests the band consists of both Pt^{2+} and Pt^{4+} emissions. For understanding the contribution of Pt in two oxidation states in detail, we analyzed the Pt $4d_{5/2}$ emission band of the sample before and after its utilization in six methane oxidation cycles (Figure 2).

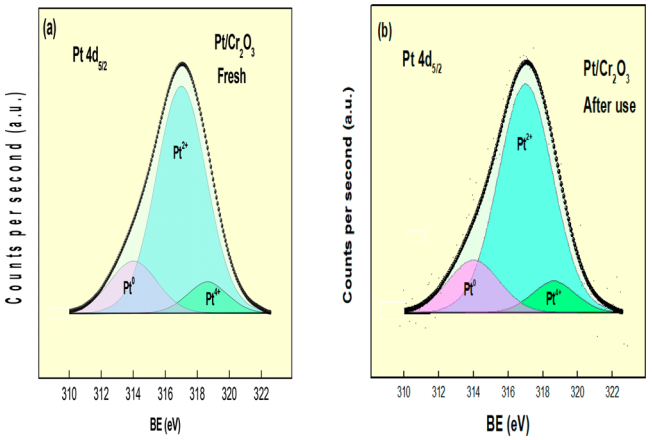

Figure 2. XPS spectra of Pt $4d_{5/2}$ emission in 1% Pt/Cr_2O_3, (a) fresh and (b) used (in six cycles of methane oxidation) 1% Pt/Cr_2O_3 catalyst.

As can be noticed in Figure 2, the Pt $4d_{5/2}$ band of both the fresh and used catalysts disclosed an intense signal at ~316.9 eV and two weak signals at 314.0 and 318.6 eV. While the 316.9 eV component corresponds to Pt^{2+}, the 314.0 and 318.6 components correspond to the Pt^0 and Pt^{4+} states, respectively.[36,37] The results clearly indicate that nearly all of the Pt atoms in the sample remain in Pt^{2+} valence state, with lesser amounts at the catalyst surface of Pt^0 and Pt^{4+} species. The XPS calculated Pt/Cr atomic ratio in the catalyst (Table 1) indicates that platinum species are covering ~30% of the Cr surface atoms. This fact suggests a high platinum dispersion on the catalyst surface, which can lead to the formation of small metallic nanoparticles.

XPS Study of the 1% Pt/ZrO_2 Catalyst. The XPS study performed on 1% Pt/ZrO_2 fresh and after its catalytic operation in six CH_4 oxidation cycles, revealed BE values and the atomic percentages of the different Pt species at the catalyst surface. These values were estimated from the Pt $4f_{7/2}$, and Zr $3d_{5/2}$ core-level emissions, as presented in Table 1. In Figure 3, it can be seen that the core level Pt $4f_{7/2}$ emission of

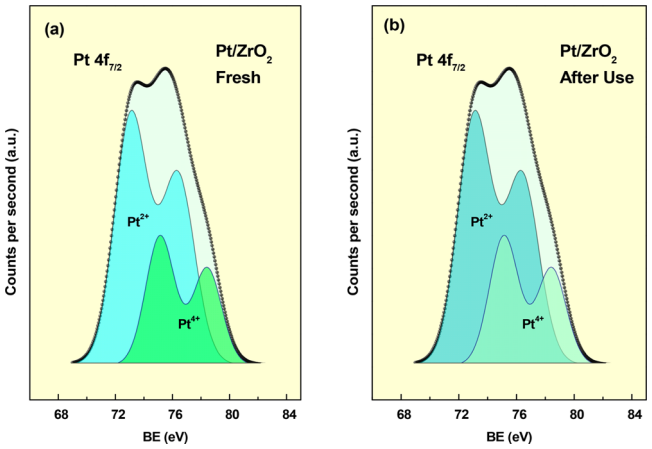

Figure 3. XPS spectra of Pt $4f_{7/2}$ emission in 1% Pt/ZrO_2: (a) fresh and (b) used (in six cycles of methane oxidation).

the freshly prepared catalyst, unveiled two components: the first one was positioned at ~73.1 eV, corresponding to Pt^{2+} oxidation state, and the second one, at ~75.3 eV, assigned to Pt^{4+}.[29,33−35] The Pt/Zr atomic ratio estimated by XPS in the fresh catalyst (Table 1) suggests that platinum species cover ~14% of the Zr surface atoms. Note that after the catalytic tests, both the intensity and shape of the Pt $4f_{7/2}$ emission band remained unchanged.

XPS Analysis of the 1% Pt/γ-Al_2O_3 Catalyst. The XPS analysis was also performed on the 1% Pt/γ-Al_2O_3 before (fresh) and after having used it for the oxidation cycles. The core level Pt 4d emissions, particularly the 4 $d_{5/2}$ peaks from the samples were analyzed, as they were easily detectable. Even though for the XPS analysis of platinum, usually Pt $4f_{7/2}$ emission band is utilized, we did not use this emission band as the Al 2p line of γ-Al_2O_3, coincides with the Pt 4f line, which makes the study more difficult. This also would have complicated the direct estimation of the platinum states. Although the Pt 4 $d_{5/2}$ emission of the catalyst was weaker, it did not overlap with the emission bands of γ-Al_2O_3.

The XPS spectra of 1% Pt/γ-Al_2O_3 before (fresh) and after having used it for the methane oxidation cycles, revealed binding energy values and atomic percentages of the Pt species in diverse oxidation states. These values were determined from the Pt $4d_{5/2}$ core level emissions and are presented in Table 1. In Figure 4, it is clear that the core level Pt $4d_{5/2}$ emission showed only one component peak positioned at ~317.2 eV. This fact indicates that Pt is present only as Pt^{2+}.[29,38,39] The Pt/Al atomic ratio, determined by XPS analysis of the fresh catalyst, indicates that platinum species cover ~30% of the total Al surface atoms. Such a high metallic dispersion at the surface of the composite catalyst indicates the formation of small metal nanoparticles.

https://doi.org/10.1021/acs.iecr.1c02902
Ind. Eng. Chem. Res. 2021, 60, 18841−18852

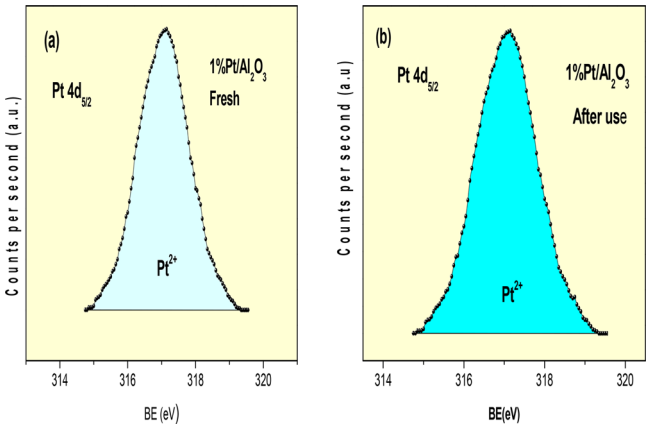

Figure 4. XPS spectra of Pt $4d_{5/2}$ emission in 1% Pt/γ-Al_2O_3: (a) fresh sample and (b) after having used it for the CH_4 oxidation cycles.

HR-TEM Study of the Catalysts. *Study of 1% Pt/Cr_2O_3.* Figure 5 shows two typical HR-TEM images of 1% Pt/Cr_2O_3

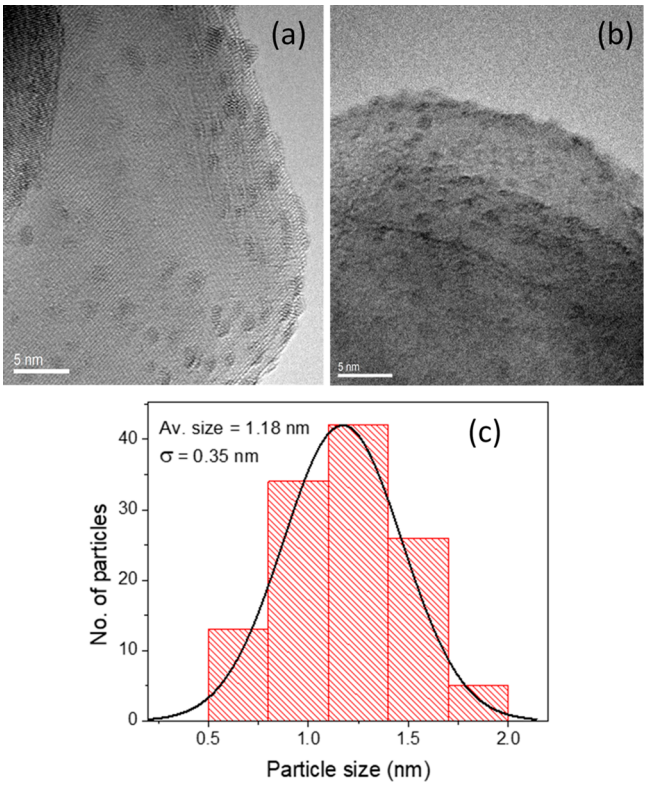

Figure 5. (a, b) Typical HR-TEM images of 1% Pt/Cr_2O_3 (fresh), and (c) size distribution histogram for the Pt particles formed over Cr_2O_3 support. The average size of the Pt particles estimated through a Gaussian fit to the size distribution histogram was ~1.18 ± 0.35 nm.

before having used it for the oxidation cycles (fresh catalyst). The images clearly revealed the formation of platinum nanoparticles over Cr_2O_3 support. The diameter of these highly dispersed Pt nanoparticles vary between 0.6 nm and 2.0 nm, with an estimated average size of ~1.18 ± 0.35 nm. As it has been reported earlier, small metal nanoparticles, formed over metal-oxide supports, can have electron defectiveness. This defectiveness is due to the interactions of the metal and the support at their interface.[40,41] This fact and the effect of catalyst calcination in air at high temperature (600 °C), justify the presence of such a high number of Pt^{x+} species at the Cr_2O_3 surface.

Study of 1% Pt/ZrO_2. Figure 6 shows two typical HR-TEM images of the freshly prepared 1% Pt/ZrO_2 catalyst. Small Pt

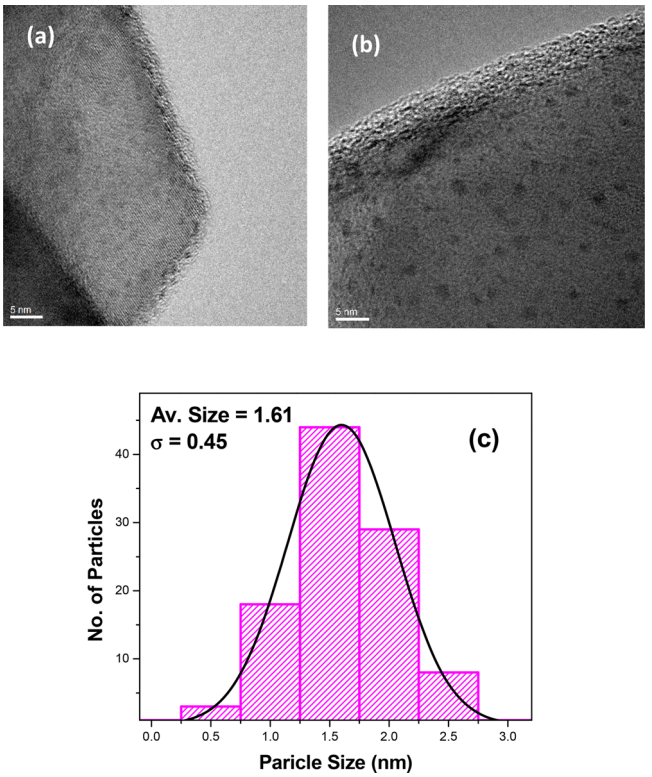

Figure 6. (a, b) Typical HR-TEM images of 1% Pt/ZrO_2 (fresh) and (c) size distribution histogram of the Pt particles formed over ZrO_2 support. The average size of the Pt particles estimated through a Gaussian fit to the size distribution histogram was ~1.61 ± 0.45 nm.

particles of spherical shape in the 1.0−2.5 nm size range can be seen in the figure. The average Pt nanoparticles size (nm) generated over ZrO_2 support was calculated from the size distribution histogram prepared by measuring the dimension of individual nanoparticles in the HR-TEM images. The estimated average size of the Pt particles formed over ZrO_2 support was ~1.61 ± 0.45 nm.

Study of 1% Pt/γ-Al_2O_3. Figure 7 presents typical HR-TEM images of the fresh 1% Pt/γ-Al_2O_3 sample. The generation of Pt nanoparticles between 2.0 nm and 5.5 nm can be seen in the images. The average size of the particles estimated from their size distribution (Figure 7c) was ~3 nm. The figure also shows these nanoparticles are less monodispersed, compared with those Pt nanoparticles generated over Cr_2O_3 and ZrO_2 supports. The Pt nanoparticles developed no well-defined lattice planes in the HR-TEM images of 1% Pt/γ-Al_2O_3 catalyst. This observation can be explained by the fact that alumina support presents an amorphous nature.

The results presented in Figures 5−7 show the effect of supports on the size distribution of the generated platinum nanoparticles. It is clearly seen that the average size of the Pt nanoparticles formed over Al_2O_3 support (~3 nm) is bigger than the average size of the Pt nanoparticles formed over Cr_2O_3 (~1.18 nm) and ZrO_2 (~1.61 nm) supports. Now, the difference in the size of Pt nanoparticles in 1% Pt/γ-Al_2O_3, 1% Pt/ZrO_2, and, 1% Pt/Cr_2O_3 catalysts cannot be due to their

https://doi.org/10.1021/acs.iecr.1c02902
Ind. Eng. Chem. Res. 2021, 60, 18841−18852

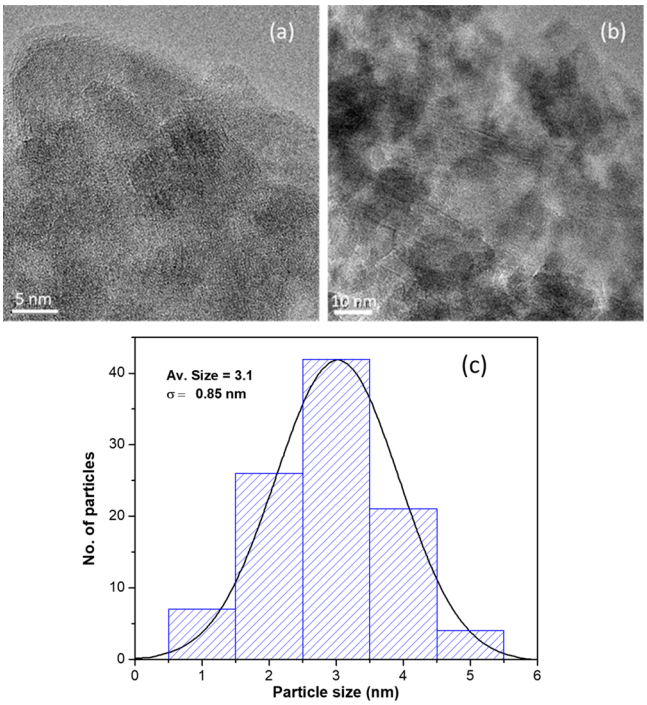

Figure 7. (a, b) Typical HR-TEM images obtained of 1% Pt/γ-Al_2O_3 (fresh) and (c) histogram of the size distribution of the Pt nanoparticles generated over Al_2O_3 support. The average size of the Pt particles estimated through a Gaussian fit to the size distribution histogram was ~3.0 ± 0.85 nm.

preparation method, because they were prepared under similar conditions. This difference is probably due to the differences in their surface energies.

Determination of Pt Dispersion in the Catalysts. The platinum dispersion (D_{Pt}) values of the catalysts were estimated from the mean size (d_{Pt}) values of the Pt nanoparticles determined from HR-TEM analysis of the three catalysts, according to eq 1:

$$D_{Pt} = \frac{6V_{Pt}}{a_{Pt}d_{Pt}} \quad (1)$$

where V_{Pt} is the Pt atomic volume and a_{Pt} is the average surface area occupied by one Pt atom. More information has been provided in the Supporting Information (in the section entitled "Platinum Dispersion Value Determination").

Equation 2 defines the Pt dispersion (D_{Pt}) value:

$$D_{Pt} = \frac{\text{number of surface Pt atoms}}{\text{number of total Pt atoms}} \quad (2)$$

The number of surface Pt atoms was estimated from eqs 1 and 2, considering a total of 3.08 × 10^{19} Pt atoms per gram of catalyst. In Table 2, the D_{Pt} values, the mean Pt nanoparticles size (d_{Pt}), and the number of Pt surface atoms per gram of catalysts is reported. In Table 2, it can be seen that 1% Pt/Cr_2O_3 and 1% Pt/ZrO_2 present similar Pt dispersion values. However, low Pt dispersion value was estimated for the 1% Pt/γ-Al_2O_3 catalyst.

Table 2. Pt Dispersion Values (Considering a Total of 3.08 × 10^{19} Pt atoms/g of Catalyst), Number of Surface Pt Atoms and Mean Size of Pt Nanoparticles in the Catalysts

Pt catalyst	d_{Pt} (nm)	Pt surface (atoms/g cat)	D_{Pt}
1% Pt/Cr_2O_3	1.18	2.80 × 10^{19}	0.93
1% Pt/ZrO_2	1.61	2.13 × 10^{19}	0.70
1% Pt/γ-Al_2O_3	3.10	1.13 × 10^{19}	0.37

Raman Spectroscopy analysis of the catalysts. As the band gap energy of the metal oxide supports such as Al_2O_3 (7.0−7.6 eV) and ZrO_2 (5.8−7.8 eV) are considerably high, we could perform the IRROA study on the Cr_2O_3 and 1% Pt/Cr_2O_3 samples only.[42,43] As the band gap energy of Cr_2O_3 (3.20−2.98 eV) and its exciton peak is at 2.945 eV (421 nm), a He−Ne laser (633 nm, 1.96 eV) was utilized for inducing IRROA signal of these samples.[44,45]

In Figure 8, it can be noticed that the Raman spectrum of the pristine Cr_2O_3 sample revealed well-defined, intense

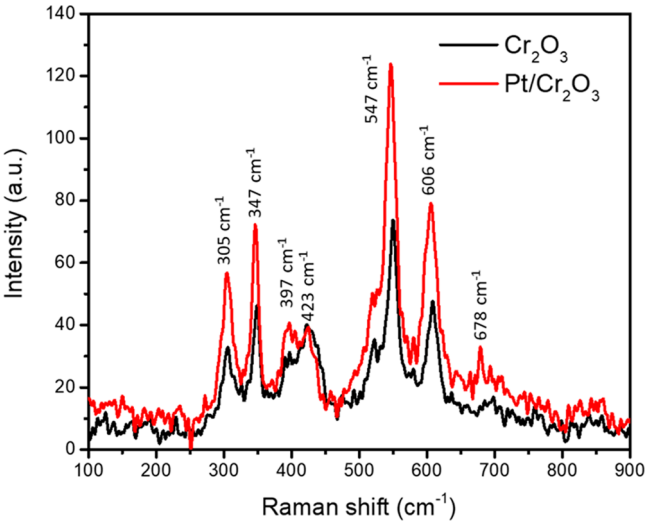

Figure 8. Room-temperature Raman spectra of the Cr_2O_3 and Pt/Cr_2O_3 catalysts recorded by exciting the samples by He−Ne (533 nm) laser.

Raman peaks at 305, 347, 397, 423, 547, 606, and 678 cm^{-1} wavenumbers. The 305, 347, 547, and 606 cm^{-1} peaks have previously been attributed to the crystalline Cr_2O_3, while the feature at 678 cm^{-1} has been assigned to the B_{2g} (ν_a) mode of highly disordered CrO_2 surface.[46−49] On the other hand, the signal appeared at ~397 cm^{-1}, corresponds to the E_g mode of Cr_2O_3 which appears with very low intensity at room temperature.[50,51]

The 1% Pt/Cr_2O_3 catalyst also revealed that all seven dispersion bands appeared in the pristine Cr_2O_3 catalyst. However, the intensity of all the dispersion bands in the composite catalyst are much higher. The enhanced intensity of all the dispersion bands in the composite catalyst corresponds to the resonance Raman optical activity in the sample induced by the dipolar moieties formed due to electron redistribution, as has been discussed later. The Raman signal amplification in the 1% Pt/Cr_2O_3 sample is controlled by the polarizability of the molecule under investigation, which is connected with the dipole moment by the relation $P = \alpha E$, where P is the induced dipole moment, α the polarizability, and E the electric field.[52] According to the Kramers−Heisenberg formula, the Raman scattering intensity is proportional to α^2E^2; the proportionality with E^2 originating from the e exciting field intensity.[53] The Raman results of the pure Cr_2O_3 and 1% Pt/Cr_2O_3 catalysts clearly indicate the formation of dipolar moieties in the composite.

https://doi.org/10.1021/acs.iecr.1c02902
Ind. Eng. Chem. Res. 2021, 60, 18841−18852

CH_4 Oxidation over the Catalysts. In Figures S1, S2, and S3 in the Supporting Information, we present the evolutions of CH_4 conversion with reaction temperature for the 1% Pt/Cr_2O_3, 1% Pt/ZrO_2, and 1% Pt/γ-Al_2O_3 composite catalysts, respectively, during the first, third, and sixth CH_4 oxidation cycles. The values quantified from the light-off curves of all the catalysts permitted the construction of Table S2 in the Supporting Information. This table lists the temperatures of 10% (T_{10}), 50% (T_{50}), and 100% (T_{100}) conversion of CH_4 in methane oxidation reactions using the catalysts. In Figure S4 in the Supporting Information, the evolutions of CH_4 conversion, as a function of reaction temperature, for the three bare supports (Cr_2O_3, ZrO_2, and Al_2O_3) during the first cycle are presented. Figure S4 and Table S2 show very small CH_4 conversion during the six cycles over the three supports in the temperature range of 25−500 °C.

Figure 9 presents the progression of CH_4 conversion with reaction temperature only during the sixth oxidation cycle for

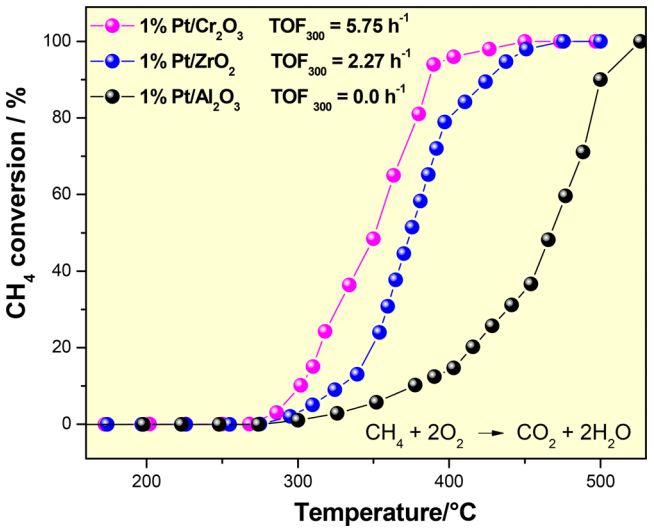

Figure 9. Evolution of CH_4 conversion, as a function of oxidation temperature during the sixth cycle over 1% Pt/Cr_2O_3, 1% Pt/ZrO_2, and 1% Pt/γ-Al_2O_3 catalysts.

1% Pt/Cr_2O_3, 1% Pt/ZrO_2, and 1% Pt/γ-Al_2O_3. This figure and the data presented in Table S2 show considerably high values for the conversion of CH_4 over 1% Pt/Cr_2O_3 and 1% Pt/ZrO_2 oxidation catalysts. Note that the T_{10}, T_{50}, and T_{100} values estimated over these two catalysts remained almost unaltered until the sixth cycle (Table S2). These results designate a very high stability of 1% Pt/Cr_2O_3 and 1% Pt/ZrO_2 for methane oxidation. The unaffected T_{10}, T_{50}, and T_{100} observed values also mean that the electronic organization of the catalysts (1% Pt/Cr_2O_3, 1% Pt/ZrO_2) persist unchanged during the reaction cycles. Figure S3 in the Supporting Information, and Figure 9, present the estimated percentage of CH_4 conversion with reaction temperature during the first, third, and sixth cycles over 1% Pt/γ-Al_2O_3 catalyst in the studied temperature range. The figure shows that the conversion of CH_4 is considerably lower for this catalyst than the methane conversion manifested by 1% Pt/Cr_2O_3 and 1% Pt/ZrO_2 catalysts. The T_{50} value determined over 1% Pt/γ-Al_2O_3 catalyst is ∼115 °C superior than that determined for 1% Pt/Cr_2O_3, and ∼90 °C higher than the one determined over 1% Pt/ZrO_2.

With the aim of comparing the intrinsic activities of the catalysts, the turnover frequencies (TOFs) were determined from the CH_4 oxidation conversion at 300 °C, as a function of the reaction time. The calculated TOFs values are listed in Table S3 in the Supporting Information. The TOF value determined at 300 °C on 1% Pt/Cr_2O_3 was about twice as high as the TOF values determined on 1% Pt/ZrO_2. The 1% Pt/γ-Al_2O_3 sample did not present methane oxidation activity at 300 °C. As can be seen in Table S3, the 1% Pt/Cr_2O_3 sample presents the highest catalytic activity for methane oxidation. It should be recalled that the utilization of chromium-based catalysts have been often avoided since Cr_2O_3 can be oxidized to CrO_3, which is potentially carcinogenic.[54] However, it has been shown that CrO_3 is thermally unstable above 250 °C, liberating oxygen and eventually transforming to Cr_2O_3.[55] So, the utilization of Cr_2O_3 support for CH_4 oxidation does not generate hazardous CrO_3 during CH_4 oxidation because the catalytic reaction occurs at high temperatures (above 300 °C).

Mechanistic Considerations of CH_4 Oxidation over 1% Pt/Cr_2O_3, 1% Pt/ZrO_2, and, 1% Pt/γ-Al_2O_3. The differences in the activities presented by the composite catalysts for methane oxidation cannot be explained only through the estimated specific surface areas of the catalysts. In Table S1 in the Supporting Information, it can be seen that the 1% Pt/Cr_2O_3 catalyst had the lowest specific surface area, although it manifested the highest methane oxidation activity (lowest light-off temperature). Moreover, the 1% Pt/γ-Al_2O_3 catalyst, bearing the highest specific surface area, manifested the lowest activity in methane oxidation. Table 1 shows that the relative atomic ratio Pt/(Cr, Zr, or Al) decreases in the following order: Pt/Cr > Pt/Al > Pt/Zr. However, the catalytic activity for methane oxidation decreases in the order: Pt/Cr > Pt/Zr > Pt/Al. Therefore, the catalytic activity of the three catalysts in methane oxidation cannot be explained by considering the atomic concentrations of metal over the supports, as determined by their XPS analysis or by the specific surface area estimated from their N_2 physisorption isotherms.

Therefore, to explain the methane oxidation behaviors of the three catalysts, we first considered the effects of the electronic states of platinum at the catalyst surface determined by their XPS analysis. The probability of adsorption of CH_4 molecules on the catalyst surface increases with the number of activated methane molecules in the reactant gas striking the catalyst surface. To be adsorbed, the molecules striking the catalyst surface must hold a total energy, in the reactant gas (E_T), as high or higher than the adsorption activation energy. The E_T of a methane molecule is the sum of its kinetic and potential energies. The kinetic energy of the methane molecules labeled as E_K is explained by the kinetic theory of gases, and the methane molecule potential energy ($U_{d\text{-}id}$), results from the interaction between the dipolar site at the catalyst surface and the induced-dipole in the CH_4 molecule. Note that the interactions between the dipolar sites of the catalyst surface and the induced dipole in the CH_4 molecule are dependent on the potential of the dipolar site and on the polarizability (α) of methane. Therefore, the total energy of a CH_4 molecule striking the catalyst surface can be determined using eqs 3 and 4:

$$E_T = E_K + U_{d-id} \tag{3}$$

$$E_T(CH_4) = \frac{3}{2}k_B T + U_{d-id} \tag{4}$$

https://doi.org/10.1021/acs.iecr.1c02902
Ind. Eng. Chem. Res. 2021, 60, 18841−18852

Table 3. Electric Dipole Potentials Estimated for the Dipoles Formed on the Surface of the Catalysts

catalytic sites (dipolar moieties)	Atomic or Ionic Radius, r_i (pm)						dipole length,[a] r (pm)	q_1-q_2 (C)	$\varphi(4\pi\varepsilon_0)$[b] (C/pm)
	Pt^0	Pt^{2+}	Pt^{4+}	Cr^{3+}	Zr^{4+}	Al^{3+}			
1% Pt/Cr_2O_3									
Pt^0-Pt^{4+}	177		76.5	75.5			253.5	4	0.0157
Pt^0-Pt^{2+}	177	94					271	2	0.0073
$Pt^{2+}-Pt^{4+}$		94	76.5				170.5	2	0.0119
Pt^0-Cr^{3+}	177			75.5			252.5	3	0.0118
$Pt^{2+}-Cr^{3+}$		94		75.5			169.5	1	0.0058
$Pt^{4+}-Cr^{3+}$			76.5	75.5			152.0	1	0.0065
1% Pt/ZrO_2									
$Pt^{2+}-Zr^{4+}$		94			73		167.0	2	0.0117
$Pt^{4+}-Zr^{4+}$			76.5		73		149.5	0	0
$Pt^{2+}-Pt^{4+}$		94	76.5				170.5	2	0.0119
1% Pt/γ-Al_2O_3									
$Pt^{2+}-Al^{3+}$		94				67.5	161.5	1	0.0061

[a] $r = r_1 + r_2$. [b] $\varphi(4\pi\varepsilon_0) = (q_1 - q_2)/r$.

where k_B is the Boltzmann constant and T is the absolute temperature. Equation 4 indicates that, for a specific temperature, the total energy of the CH_4 molecule is directly proportional to its $U_{d\text{-}id}$, which is dependent on the potential of the surface dipolar site and on the polarizability of the CH_4 molecule (which is a constant). Consequently, the CH_4 adsorption rate will increase proportionally with the increase in the potential of the dipolar sites.

The potentials of the dipolar sites at the surface of the catalysts were calculated using eq 5:

$$\varphi = \frac{q_1 - q_2}{4\pi\varepsilon_0 r} \tag{5}$$

where q_1 and q_2 are the charges on the first and second ions of the surface dipole, respectively, r is the sum of the first and second charged species, and ε_0 is the vacuum permittivity. Table 3 shows the estimated values of the potentials of the electric dipoles, formed by the surface charged species. All the dipolar sites can polarize CH_4 molecule, weakening the bond energy between C and H atoms and improving its heterolytic splitting, thereby improving the abstraction of the first hydrogen on the adsorbed molecule, which is the rate-determining step of CH_4 oxidation, and follows Reaction R2:

$$(Pt^x - Pt^y) + CH_4 \rightarrow (Pt^x)H^+ + (Pt^y)CH_3^- \tag{R2}$$

Therefore, the potential of the surface dipolar sites is a very strong factor that governs the catalytic activity for methane oxidation.

1% Pt/Cr_2O_3 Study. The XPS spectrum of the 1%Pt/Cr_2O_3 catalyst surface revealed the presence of Pt^0, Pt^{2+}, and Pt^{4+} ionic species. Presence of such ionic species on the catalyst surface can produce very stable catalytic sites of dipolar nature, consisting of adjacent Pt^x and Pt^y ions. In fact, the presence of Pt^0, Pt^{2+}, and Pt^{4+} ionic species at the catalyst surface can generate Pt^0-Pt^{4+}, Pt^0-Pt^{2+}, and $Pt^{4+}-Pt^{2+}$ dipoles. In addition, several other dipolar sites such as Pt^0-Cr^{3+}, $Pt^{2+}-Cr^{3+}$, and $Pt^{4+}-Cr^{3+}$ consisting of adjacent ionic Pt species and Cr^{3+} can be formed at the platinum/support interface.

The XPS analysis (Table 1) of the sample revealed that ~80% of the Pt surface atoms are in the Pt^{2+} oxidation state, 12% are in the Pt^0 oxidation state, and 8% are in the Pt^{4+} oxidation state. From these data and considering 2.8×10^{19} atoms/g catalyst as 100% of the Pt surface atoms (determined from HRTEM analysis, Table 2), the number of Pt surface atoms in each of the different oxidation states was determined, as shown in Table 4. Therefore, the probable number of

Table 4. Estimation of the Probable Number of Pt^x-Pt^y Surface Dipoles Generated at the Surface of 1% Pt/Cr_2O_3 and 1% Pt/ZrO_2 Catalysts, Considering a Total of 2.80×10^{19} Pt atoms/g for 1% Pt/Cr_2O_3 and a Total of 2.13×10^{19} Pt atoms/g for 1% Pt/ZrO_2[a]

Surface Pt^δ Component (%)			Number of Pt^δ Surface Atoms/g Catalyst ($\times 10^{19}$)			Number Pt^x-Pt^y Surface Dipoles/g Catalyst ($\times 10^{18}$)		
Pt^0	Pt^{2+}	Pt^{4+}	Pt^0	Pt^{2+}	Pt^{4+}	Pt^0/Pt^{2+}	Pt^0/Pt^{4+}	Pt^{2+}/Pt^{4+}
1% Pt/Cr_2O_3								
12	80	8	0.33	2.24	0.22	3.3	2.2	2.2
1% Pt/ZrO_2								
0	69	31	0	1.46	0.66	0	0	6.6

[a] The percentage of Pt^0, Pt^{2+}, and Pt^{4+} components were estimated from the XPS analysis of the catalysts.

dipoles generated between two Pt atoms in different oxidation states could be determined by the smallest number of any of the two different Pt atoms forming the dipole, as it can be seen in Table 4. In this table, it can be noticed that the probable number of the Pt^x-Pt^y dipoles formed on the surface of the 1% Pt/Cr_2O_3 catalyst is substantially high.

The electric dipole potential values presented in Table 3 indicate that the highest electric dipole potential calculated for the three catalysts corresponds to Pt^0-Pt^{4+} dipoles, which are detected only at the 1% Pt/Cr_2O_3 surface. The highest probability of CH_4 polarization is observed at these dipolar sites. This fact and the presence of the high number of these surface dipoles (2.2×10^{18}/g cat) could explain the lowest T_{10}, T_{50}, and T_{100} values of 1% Pt/Cr_2O_3 among the three composite catalysts for methane oxidation.

As can be noticed in Table 3, the dipolar moieties such as $Pt^{2+}-Pt^{4+}$, $Pt^{2+}-Cr^{3+}$, and Pt^0-Cr^{3+} also present high electric dipole potentials. Therefore, contributions of these dipolar sites on methane oxidation cannot be ruled out. Since the XPS analysis (Table 1) of the sample revealed that ~80% of the Pt surface atoms are in the Pt^{2+} oxidation state, the contribution

https://doi.org/10.1021/acs.iecr.1c02902
Ind. Eng. Chem. Res. 2021, 60, 18841−18852

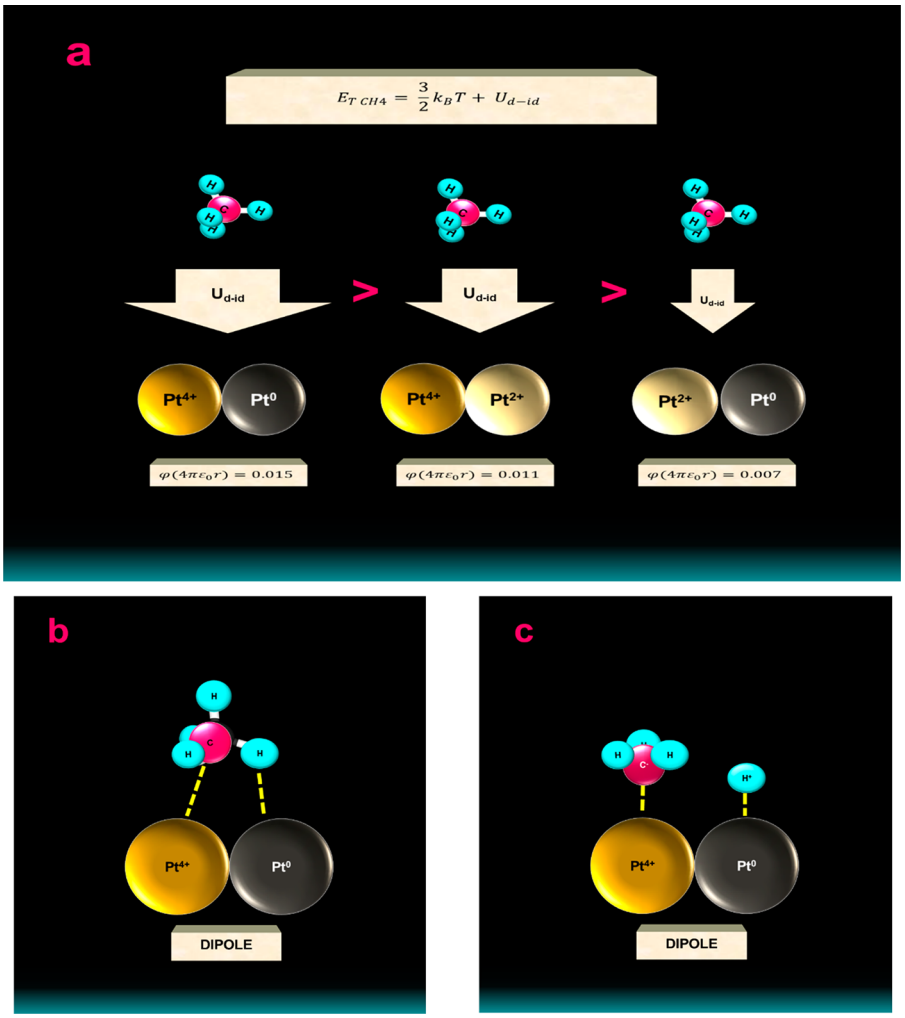

Figure 10. Schematics of the CH_4 adsorption over dipolar sites at the surface of the catalysts. (a) CH_4 in gas phase and different dipolar sites at the surface of Pt nanoparticles; (b) CH_4 polarization by Pt^0−Pt^{4+} site and generation of a transition state; and (c) hydrogen abstraction from the adsorbed CH_4 molecule.

of Pt^{2+}−Pt^{4+} and Pt^{2+}−Cr^{3+} dipolar moieties in methane oxidation can be substantial.

1% Pt/ZrO_2 Study. The effects of 1% Pt/ZrO_2 catalyst on CH_4 oxidation can be explained in a similar way as the effects of 1% Pt/Cr_2O_3 catalyst. XPS analysis of the fresh 1% Pt/ZrO_2 catalyst revealed the presence of Pt^{2+} and Pt^{4+} species at its surface. Therefore, the dipolar sites that can be generated at its surface are Pt^{2+}−Pt^{4+} and Pt^{2+}−Zr^{4+}, which can strongly polarize methane molecules. As can be noticed in Table 3, the Pt^{2+}−Pt^{4+} dipole has higher electric dipole potential than the Pt^{2+}−Zr^{4+} dipole, and, hence, it is the most active catalytic moiety at the surface of the 1% Pt/ZrO_2 catalyst, although a contribution of the Pt^{2+}−Zr^{4+} dipolar site on methane oxidation cannot be ruled out. XPS analysis of the sample (Table 1) revealed ∼69% of the Pt surface atoms in Pt^{2+} oxidation state, which indicates a high number of Pt^{2+} ions interacting with Pt^{4+} or Zr^{4+} ions. The estimated probable number of Pt^{2+}−Pt^{4+} surface dipoles/g catalyst is 0.66×10^{19} as indicated in Table 4. The presence of $Pt^{+\delta}$ species in high concentration at the surface of 1% Pt/ZrO_2 catalyst can be explained (exactly as it was explained for 1% Pt/Cr_2O_3) by the fact that the calcination temperature of the catalyst was 600 °C in air prior to being used in the methane oxidation study.

1% Pt/γ-Al_2O_3 Study. 1% Pt/γ-Al_2O_3 catalyst calcination was also performed at 600 °C in air. However, XPS analysis of the sample (Table 1) revealed almost 100% of Pt^{2+} surface species at its surface, with no trace of other ionic species. Therefore, generation of a dipolar (Pt^x−Pt^y) catalytic site at the surface of this composite catalyst did not occur. In the absence of any dipolar moiety at the surface of the catalyst, CH_4 molecules were not polarized; therefore, the activation of the C−H bond in the temperature range utilized for CH_4 oxidation cycles did not occur and the catalytic activity of this catalyst was not improved (see Table S2).

In Figure 10, we schematically present the proposed mechanism for CH_4 adsorption on the different dipolar sites at the catalyst surface. Further interactions of CH_3^-, H^+ and oxygen adsorbed at the Pt nanoparticles surface and at the Pt/support interface, may lead to the final products: CO_2 and H_2O molecules.

In order to explain the generation of Pt^x−Pt^y dipolar sites at the surface of 1% Pt/Cr_2O_3 and 1% Pt/ZrO_2 catalysts and the absence of any dipole at the surface of 1% Pt/γ-Al_2O_3, we considered the semiconducting properties of Cr_2O_3, ZrO_2, the insulating nature of γ-Al_2O_3, and the subsequent. process of electron exchanges at the metal/metal-oxide interfaces.

https://doi.org/10.1021/acs.iecr.1c02902
Ind. Eng. Chem. Res. 2021, 60, 18841−18852

Such electron transferences at metal/metal-oxide interfaces result in a change in the alignment of energy levels.[27] In Table S4 in the Supporting Information, the work function values of the catalyst components are reported.

From the electronic point of view, since the work-function value reported for Pt^0 (6.3 eV) is higher than the work-function value reported for Cr_2O_3 (5.6 eV), there is a strong probability of electron injection from Cr_2O_3 to Pt nanoparticles (Pt^0) formed over its surface, which enhances the stability of Pt^0 at the Pt/Cr_2O_3 interface, despite the fact that, during preparation, the catalyst was calcined in air at 600 °C, the strong oxidizing conditions of methane oxidation reaction and the small size of the surface Pt nanoparticles, which are favorable conditions for the formation of Pt^{2+} and Pt^{4+}.

Also, in light of the energy level alignment, the work function of Pt^0 (6.3 eV) being lower related to ZrO_2 (6.68 eV), electron injection might have occurred from Pt to ZrO_2 at the Pt/ZrO_2 interface, preventing the formation of Pt^0 species.[56] It also facilitated the formation of Pt^{2+} and Pt^{4+} species at the surface of ZrO_2 during the calcination of the catalyst at 600 °C in air during its preparation. Moreover, the electronic transfer from very small Pt nanoparticles to ZrO_2 may have contributed to the generation of stable Pt^{2+} and Pt^{4+} species at the metal/metal oxide interface, generating stable Pt^{2+}–Pt^{4+} and Pt^{2+}–Zr^{4+} dipolar sites.

On the other hand, since the γ-Al_2O_3 is an insulator, it is unable to inject electrons into Pt cores, or to receive electrons from Pt nanostructures formed over its surface. Thus, the Pt^{2+} electronic state may have been generated, during the catalyst calcination process, only through the interaction of gaseous oxygen and platinum species at the catalyst surface at 600 °C. Since the formation of any dipolar (Pt^x–Pt^y) moiety at the Pt nanoparticles surface (in 1% Pt/γ-Al_2O_3) is improbable, polarization of the CH_4 molecule also is improbable and, therefore, activation of the C–H bond is improbable. As a result, CH_4 oxidation occurs only at very high temperatures.

It is necessary to point out that, although the energy alignment between platinum and the semiconductor controls the generation of Pt ions at the semiconductor surface, the size of Pt clusters/particles, along with the support's crystallographic positioning and the preparation process of the catalyst, determine the electronic state of Pt in the composite catalyst. In this work, the CH_4–O_2 reaction was performed in excess oxygen at a temperature range of 25–500 °C. Under these conditions, the surface of platinum nanoparticles should have been entirely masked by oxygen molecules present in the reaction gas, hindering CH_4 adsorption. Notwithstanding, CH_4 molecules adsorption, at the dipolar sites on the catalyst surface, occurred; therefore, the oxidation reaction occurred. To explain this observation, we must consider eq 3. According to this equation, CH_4 molecules, because of their nonzero polarizability, are adsorbed at the dipolar sites faster than O_2 molecules, which are not polarizable, because of their null polarizability.[57] Therefore, O_2 molecules remain unaffected by the electric dipolar potential produced by the surface dipolar sites. Logically, the O_2 total energy (E_T) will not include the potential energy contribution ($U_{d\text{-}id}$), as indicated in eq 6:

$$E_T(O_2) = \frac{3}{2}k_B T \qquad (6)$$

CONCLUSIONS

The results obtained in this study clearly indicate that the catalytic activity of platinum-supported metal oxide catalysts can be controlled, by regulating the nature and the concentration of the surface (Pt^x–Pt^y) dipolar catalytic sites. On the other hand, the catalytic activity of these dipolar sites relies on the relative values of x and y, which can be controlled by a judicial selection of the semiconductor support (with suitable work function) to generate a maximum dipole moment at the catalytic sites.

ASSOCIATED CONTENT

Supporting Information

The Supporting Information is available free of charge at https://pubs.acs.org/doi/10.1021/acs.iecr.1c02902.

Methane conversion as a function of reaction temperature during the 1st, 2nd, and 6th cycle over 1% Pt/Cr_2O_3, 1% Pt/ZrO_2, and, 1% Pt/γ-Al_2O_3 catalysts; methane conversion as a function of temperature during the 1st cycle over Cr_2O_3, ZrO_2, and γ-Al_2O_3 catalysts; details of platinum dispersion value determination; the specific surface area of the catalysts before and after their use in methane oxidation cycles; T_{10}, T_{50}, and T_{100} values for methane oxidation over the catalysts; CH_4 oxidation rates (P = 1 atm, T = 300 °C, $CH_4/O_2/N_2$ = 0.2/10/89.8; 5.35 × 10^{-4} mol CH_4/h); work function values of the catalysts' components (PDF)

AUTHOR INFORMATION

Corresponding Author

Grisel Corro – *Instituto de Ciencias, Benemérita Universidad Autónoma de Puebla, 72000 Puebla, México;* orcid.org/0000-0002-7645-4477; Email: griselcorro@yahoo.com

Authors

Jorge Cruz-Mérida – *Instituto de Ciencias, Benemérita Universidad Autónoma de Puebla, 72000 Puebla, México;* orcid.org/0000-0002-7607-508X

Daniel Montalvo – *Instituto de Ciencias, Benemérita Universidad Autónoma de Puebla, 72000 Puebla, México*

Umapada Pal – *Instituto de Física, Benemérita Universidad Autónoma de Puebla, 72570 Puebla, Pue, México;* orcid.org/0000-0002-5665-106X

Complete contact information is available at: https://pubs.acs.org/10.1021/acs.iecr.1c02902

Notes

The authors declare no competing financial interest.

ACKNOWLEDGMENTS

The authors are pleased to acknowledge the Secretaría de Energía-Consejo Nacional de Ciencia y Tecnología (Cluster Biodiesel Avanzado No. FSE 250014), Mexico, and the Vicerrectoria de Investigación y Estudios de Posgrado (VIEP), BUAP (Proyect No. 2021), for their financial supports.

DEDICATION

This work is dedicated to our great friend and collaborator Prof. José Luis García Fierro, who is no longer with us.

REFERENCES

(1) Ciuparu, M. R.; Lyubovsky, M. R.; Altman, E.; Pfefferle, L. D.; Datye, A. Catalytic Combustion of Methane over Palladium-Based Catalysts. *Catal. Rev.: Sci. Eng.* **2002**, *44* (4), 593−649.

(2) A NaturalGas.org: http://naturalgas.org/overview/background (Accessed on Oct. 4, 2021).

(3) Horn, R.; Schlögl, R. Methane Activation by Heterogeneous Catalysis. *Catal. Lett.* **2015**, *145*, 23−39.

(4) Chin, Y.-H.; Buda, C.; Neurock, M.; Iglesia, E. Reactivity of chemisorbed oxygen atoms and their catalytic consequences during CH_4-O_2 catalysis on supported Pt clusters. *J. Am. Chem. Soc.* **2011**, *133*, 15958−15978.

(5) Boucher, O.; Folberth, G. A. New directions: atmospheric methane removal as a way to mitigate climate change. *Atmos. Environ.* **2010**, *44*, 3343−3345.

(6) Carother, F. P.; Schultz, H. L.; Talkington, C. *Enviromental Protection Agency*: Washington, DC, 2003.

(7) Mohr, S. H.; Evans, G. M. Long Term Forecasting of Natural Gas Production. *Energy Policy* **2011**, *39* (9), 5550−5560.

(8) Burch, R.; Urbano, F. J. Investigation of the Active State of Supported Palladium Catalysts in the Combustion of Methane. *Appl. Catal., A* **1995**, *124* (1), 121−138.

(9) Yoshida, H.; Nakajima, T.; Yazawa, Y.; Hattori, T. Support Effect on Methane Combustion over Palladium Catalysts. *Appl. Catal., B* **2007**, *71* (1−2), 70−79.

(10) Lampert, J. K.; Kazi, M. S.; Farrauto, R. J. Palladium Catalyst Performance for Methane Emissions Abatement from Lean Burn Natural Gas Vehicles. *Appl. Catal., B* **1997**, *14* (3−4), 211−223.

(11) Gélin, P.; Urfels, L.; Primet, M.; Tena, E. Complete Oxidation of Methane at Low Temperature over Pt and Pd Catalysts for the Abatement of Lean-Burn Natural Gas Fuelled Vehicles Emissions: Influence of Water and Sulphur Containing Compounds. *Catal. Today* **2003**, *83* (1−4), 45−57.

(12) Hoyos, L. J.; Praliaud, H.; Primet, M. Catalytic Combustion of Methane over Palladium Supported on Alumina and Silica in Presence of Hydrogen Sulfide. *Appl. Catal., A* **1993**, *98* (2), 125−138.

(13) Raj, A. Methane Emission Control. *Johnson Matthey Technol. Rev.* **2016**, *60* (4), 228−235.

(14) Tao, F. F.; Shan, J.-j.; Nguyen, L.; Wang, Z.; Zhang, S.; Zhang, L.; Wu, Z.; Huang, W.; Zeng, S.; Hu, P. Understanding Complete Oxidation of Methane on Spinel Oxides at a Molecular Level. *Nat. Commun.* **2015**, *6*, 7798.

(15) Farrauto, R. J. Low-temperature oxidation of methane. *Science* **2012**, *337* (6095), 659−660.

(16) Yang, J.; Guo, Y. B. Nanostructured Perovskite Oxides as Promising Substitutes of Noble Metals Catalysts for Catalytic combustion of Methane. *Chin. Chem. Lett.* **2018**, *29* (2), 252−260.

(17) Zhang, Y.; Glarborg, P.; Johansen, K.; Andersson, M. P.; Torp, T. K.; Jensen, A. D.; Christensen, J. M. A Rhodium-Based Methane Oxidation Catalyst with High Tolerance to H_2O and SO_2. *ACS Catal.* **2020**, *10*, 1821−1827.

(18) Hicks, R. F.; Qi, H.; Young, M. L.; Lee, R. G. Structure sensitivity of methane oxidation over platinum and palladium. *J. Catal.* **1990**, *122*, 280−294.

(19) Ribeiro, F. H.; Chow, M.; Dallabetta, R. A. Kinetics of the complete oxidation of methane over supported palladium catalysts. *J. Catal.* **1994**, *146*, 537−544.

(20) Kylhammar, L.; Carlsson, P. A.; Skoglundh, M. Sulfur promoted low-temperature oxidation of methane over ceria supported platinum catalysts. *J. Catal.* **2011**, *284*, 50−59.

(21) Burch, R.; Loader, P. K.; Urbano, F. J. Some Aspects of Hydrocarbon Activation on Platinum Group Metal Combustion Catalysts. *Catal. Today* **1996**, *27* (1−2), 243−248.

(22) Carlsson, P.-A.; Nordström, M.; Skoglundh, M. Virtual Control for High Conversion of Methane Over Supported Pt. *Top. Catal.* **2009**, *52*, 1962.

(23) Carlsson, P.-A.; Fridell, E.; Skoglundh, M. Methane Oxidation Over Pt/Al_2O_3 and Pd/Al_2O_3 Catalysts Under Transient Conditions. *Catal. Lett.* **2007**, *115* (1−2), 1−7.

(24) Becker, E.; Carlsson, P.-A.; Grönbeck, H.; Skoglundh, M. Methane Oxidation Over Alumina Supported Platinum Investigated by Time-Resolved in situ XANES Spectroscopy. *J. Catal.* **2007**, *252* (1), 11−17.

(25) Becker, E.; Carlsson, P.-A.; Kylhammar, L.; Newton, M. A.; Skoglundh, M. In Situ Spectroscopic Investigation of Low-Temperature Oxidation of Methane over Alumina-Supported Platinum During Periodic Operation. *J. Phys. Chem. C* **2011**, *115* (4), 944−951.

(26) Zhdanov, V. P.; Carlsson, P.-A.; Kasemo, B. Simulation of Methane Oxidation on Pt. *J. Chem. Phys.* **2007**, *126* (23), 234705.

(27) Greiner, M. T.; Helander, M. G.; Tang, W.-M.; Wang, Z.-B.; Qiu, J.; Lu, Z.-H. Universal Energy-Level Alignment of Molecules on Metal Oxides. *Nat. Mater.* **2012**, *11*, 76−81.

(28) Ma, Y.; Wang, L.; Liu, Z.; Cheng, R.; Zhong, L.; Yang, Y.; He, X.; Fang, Y.; Terano, M.; Liu, B. High-resolution XPS and DFT Investigations Into Al-modified Phillips CrOx/SiO2 Catalysts. *J. Mol. Catal. A: Chem.* **2015**, *401*, 1−12.

(29) Briggs, D., Seah, M. P., Eds. *Practical Ssurface Analysis by Auger and X-ray Photoelectron Spectroscopy*, 2nd Edition; Wiley: Chichester, U.K., 1990.

(30) Fang, Y.; Liu, B.; Terano, M. Photo-Sstability of Surface Cchromate Species on Phillips CrO_x/SiO_2 Catalysts Isothermally Calcined at Various Temperatures, Probed by High Resolution X-ray Photoelectron Spectroscopy. *Appl. Catal., A* **2005**, *279* (1−2), 131−138.

(31) Drawdy, J. E.; Hoflund, G. B.; Gardner, S. D.; Yngvadottir, E.; Schryer, D. R. Effect of Pretreatment on a Platinized Tin Ooxide Catalyst Used for Low Temperature Co Oxidation. *Surf. Interface Anal.* **1990**, *16*, 369−374.

(32) Jackson, S. D.; Willis, J.; McLellan, G. D.; Webb, G.; Keegan, M. B. T.; Moyes, R. B.; Simpson, S.; Wells, P. B.; Whyman, R. Supported Metal Catalysts: Preparation, Characterization, and Function: I. Preparation and Physical Characterization of Platinum Catalysts. *J. Catal.* **1993**, *139* (1), 191−206.

(33) Kim, K. S.; Winograd, N.; Davis, R. E. Electron spectroscopy of platinum-oxygen surfaces and application to electrochemical studies. *J. Am. Chem. Soc.* **1971**, *93* (23), 6296−6297.

(34) Arico, A. S.; Shukla, A. K.; Kim, H.; Park, S.; Min, M.; Antonucci, V. An XPS Study on Oxidation States of Pt and its Alloys with Co and Cr and its Relevance to Electroreduction of Oxygen. *Appl. Surf. Sci.* **2001**, *172* (1−2), 33−44.

(35) Barr, T. L.; Yin, M. P. Studies of Pt Metal Catalysis by High-Resolution Electron Microscopy for Chemical Analysis. Characterization and Catalyst Development. *ACS Symp. Ser.* **1989**, *411* (ch19), 203−213.

(36) Wang, X.; Yu, H.; Hua, D.; Zhou, S. Enhanced Catalytic Hydrogenation Activity and Selectivity of Pt-M_xO_y/AL_2O_3 (M = Ni, Fe, Co) Heteroaggregate Catalysts by in situ Transformation of PtM Alloy Nanoparticles. *J. Phys. Chem. C* **2013**, *117* (14), 7294−7302.

(37) Escard, J.; Pontvianne, B.; Chenebaux, M. T.; Cosyns, J. *Bull. Soc. Chim. Fr.* **1975**, 2400.

(38) Zsoldos, Z.; Guczi, L. Structure and Catalytic Activity of Alumina Supported Platinum-Cobalt Bimetallic Catalysts. Effect of Treatment on the Interface Layer. *J. Phys. Chem.* **1992**, *96* (23), 9393−9400.

(39) Guczi, L.; Sárkány, A.; Koppány, Z. Mechanism of the decomposition of Pt—Co bimetallic particles in NaY zeolites. *Appl. Catal., A* **1994**, *120* (1), L1−L5.

(40) Ahmadi, M.; Mistry, H.; Roldan Cuenya, B. Tailoring the Catalytic Properties of Metal Nanoparticles Via Support Interactions. *J. Phys. Chem. Lett.* **2016**, *7* (17), 3519−3533.

(41) Cargnello, M.; Doan-Nguyen, V. V. T.; Gordon, T. R.; Diaz, R. E.; Stach, E. A.; Gorte, R. J.; Fornasiero, P.; Murray, C. B. Control of Metal Nanocrystal Size Reveals Metal-Support Interface Role for Ceria Catalysts. *Science* **2013**, *341*, 771−773.

(42) Filatova, E. O.; Konashuk, A. S. Interpretation of the Changing the Band Gap of Al_2O_3 Depending on its Crystalline Form: Connection with Different Local Symmetries. *J. Phys. Chem. C* **2015**, *119*, 20755−20761.

https://doi.org/10.1021/acs.iecr.1c02902
Ind. Eng. Chem. Res. 2021, 60, 18841−18852

(43) Garcia, J. C.; Scolfaro, L. M.; Lino, A. T.; Freire, V. N.; Farias, G. A.; Silva, C. C.; Leite Alves, H. W.; Rodrigues, S. C. P.; da Silva, E. F. Structural, electronic, and optical properties of ZrO_2 from ab initio calculations. *J. Appl. Phys.* **2006**, *100*, 104103.
(44) Gionco, C.; Hernandez, S.; Castellino, M.; Gadhi, T. A.; Munoz-Tabares, J. A.; Cerrato, E.; Tagliaferro, A.; Russo, N.; Paganini, M. C. Synthesis and characterization of Ce and Er doped ZrO_2 nanoparticles as solar light driven photocatalysts. *J. Alloys Compd.* **2019**, *775*, 896−904.
(45) Abdullah, M. M.; Rajab, F. M.; Al-Abbas, S. M. Structural and optical characterization of Cr_2O_3 nanostructures: Evaluation of its dielectric properties. *AIP Adv.* **2014**, *4*, 027121.
(46) Yang, J.; Martens, W. N.; Frost, R. L. Transition of chromium oxyhydroxide nanomaterials to Chromium oxide: a hot-stage Raman spectroscopic study. *J. Raman Spectrosc.* **2011**, *42*, 1142−1146.
(47) Hatch, J. J.; Gewirth, A. A. J. Electrochem. Soc.Potential dependent chromate adsorption on gold. *J. Electrochem. Soc.* **2009**, *156*, D497.
(48) Ivanova, T.; Gesheva, K. A.; Kozlov, M.; Abrashev, M. Electrochemic and Optical Study of Atmospheric Pressure Chemical Vapour Deposition MoO_3 - Cr_2O_3 Films. *J. Nanosci. Nanotechnol.* **2011**, *11*, 8017−8023.
(49) Baranov, A. V.; Bogdanov, K. V.; Fedorov, A. V.; Yarchuk, M. V.; Ivanov, A. I.; Veiko, V. P.; Berwick, K. Micro-Raman characterization of laser-induced local thermo-oxidation of thin chromium films. *J. Raman Spectrosc.* **2011**, *42*, 1780.
(50) Beattie, R.; Gilson, T. R. The single-crystal Raman spectra of nearly opaque materials. Iron (III) oxide and chromium (III) oxide. *J. Chem. Soc. A* **1970**, *5*, 980.
(51) Shim, S.-H.; Duffy, T. S.; Jeanloz, R.; Yoo, C.-S.; Iota, V. Raman spectroscopy and x-ray diffraction of phase transitions in Cr_2O_3 to 61 GPa. *Phys. Rev. B: Condens. Matter Mater. Phys.* **2004**, *69*, 144107.
(52) Teodorescu, C. M. Image molecular dipoles in Surface Enhanced Raman Scattering. *Phys. Chem. Chem. Phys.* **2015**, *17*, 21302.
(53) Kramers, H. A.; Heisenberg, W. Emission Intensity in Hydrogen Atom Calculated from a Non-Probabilistic Approach to the Electron Transitions. *Z. Phys.* **1925**, *31*, 681−708.
(54) Katz, S. A.; Salem, H. The toxicology of chromium with respect to its chemical speciation: a review. *J. Appl. Toxicol.* **1993**, *13*, 217−224.
(55) Mosesman, M. A. Stability of Chromium Oxides. *J. Am. Chem. Soc.* **1954**, *76*, 295−296.
(56) Li, H.; Wu, Y.; Li, C.; Gong, Y.; Niu, L.; Liu, X.; Jiang, Q.; Sun, C.; Xu, S. Design of Pt/t-ZrO_2/g-C_3N_4 Efficient Photocatalyst for the Hydrogen Evolution Reaction. *Appl. Catal., B* **2019**, *251*, 305−312.
(57) Ozier, I. Ground-State Electric Dipole Moment of Methane. *Phys. Rev. Lett.* **1971**, *27*, 1329−1335.

https://doi.org/10.1021/acs.iecr.1c02902
Ind. Eng. Chem. Res. 2021, 60, 18841−18852